Physics of the Earth and Planetary Interiors 245 (2015) 59–70

Contents lists available at ScienceDirect

Physics of the Earth and Planetary Interiors

journal homepage: www.elsevier.com/locate/pepi

Long-term evolution of intraplate seismicity in stress shadows after a megathrust

Tae-Kyung Hong *, Junhyung Lee, Soung Eil Houng

Yonsei University, Department of Earth System Sciences, 50 Yonsei-ro, Seodaemun-gu, Seoul 120-749, South Korea

ARTICLE INFO

Article history:
Received 14 August 2014
Received in revised form 18 May 2015
Accepted 29 May 2015
Available online 6 June 2015

Keywords:
Long-term seismicity
Tohoku-Oki earthquake
Stable intraplate region
Stress shadow
Earthquake swarm
Seismicity change
Megathrust

ABSTRACT

Megathrusts produce large permanent lithospheric displacements as well as strong transient ground shaking up to regional distances. The influence of the 2011 M9.0 Tohoku-Oki earthquake on the seismicity in stable intraplate regions around the Korean Peninsula is investigated. The differential lateral displacements by the megathrust build transient radial tension field over the backarc lithosphere, constructing stress shadows for all types of faults in optimal orientation over the wide backarc region including the southern Korean Peninsula. A characteristic seismic-velocity decrease after the megathrust supports the medium relaxation. The number of earthquakes with magnitudes greater than or equal to 2.5 was increased by 61% after the megathrust. The earthquakes occurred episodically. A series of unusual earthquake swarms and a temporal cluster of moderate-size earthquakes were observed in the Yellow Sea region. The significant seismicity increase since the megathrust may be due to the fluid diffusion during the transient tension field and the pore-fluid pressure increase during the ambient compressional-stress field recovery by tectonic loading. The induced seismicity may continue until the ambient stress field is fully recovered.

1. Introduction

Major cities with high populations are placed in intraplate regions where lithostatic stress induces diffused shallow seismicity (Sykes, 1978; Mooney et al., 2012; Choi et al., 2012; Hong and Choi, 2012). Stable intraplate regions display characteristics of low seismicity rates and long recurrence intervals. Static stress levels in many intraplate regions are close to critical thresholds for earthquake occurrence due to long-term tectonic loading. Anomalous intraplate earthquakes can occur as a consequence of local stress perturbation (Talwani, 2014). A fractional stress increment may cause a significant change in background seismicity (Stein, 1999). It is known that devastating earthquakes with long recurrence intervals occurred in intraplate regions historically (e.g., Houng and Hong (2013), Talwani (2014)). There is a concern to have such devastating earthquakes to be clock-advanced by great earthquakes.

The earth experienced three great earthquakes with magnitudes greater than or equal to 8.8 since 2004. The mechanical responses of the earth to the great earthquakes were investigated to understand the influence of the great earthquakes (West et al., 2005; Lei et al., 2011; Miyazawa, 2011; Gonzalez-Huizar et al., 2012; Lee and Hong, 2014). Dynamic triggering of microearthquakes was widely observed in active tectonic regions up to tens of thousands of kilometers (Hill et al., 1993; West et al., 2005; Durand et al., 2010; Peng and Gomberg, 2010; Lei et al., 2011; Miyazawa, 2011; Shelly et al., 2011; Wu et al., 2011; Gonzalez-Huizar et al., 2012). In addition, megathrusts accompany large regional stress changes, causing subsequent changes in seismicity properties.

There is strong correlation between stress changes and seismicity rate changes (e.g., Toda and Stein (2003) and Ma et al. (2005)). It was argued that static stress changes may cause a large seismicity rate change, particularly in the areas of high background seismicity (Stein, 1999; Toda and Enescu, 2011; Mallman and Parsons, 2008). Large earthquakes may occur in the optimally-oriented faults as a consequence of static stress change (King et al., 1994; Freed and Lin, 2001). Faults in near-critical conditions (close to failure stresses) may respond preferentially to the stress changes. However, the seismicity changes for static stress changes are not observed consistently. Some studies report no apparent correlations between static stress changes and seismicity changes (e.g., Felzer and Brodsky (2005) and Mallman and Zoback (2007)).

The seismicity changes for dynamic stress changes were studied widely in regional and teleseismic distances (e.g., Kilb et al. (2000), Freed (2005), and Brodsky and van der Elst (2014)). On the other hand, the seismicity changes for static stress changes were studied

* Corresponding author.
E-mail address: tkhong@yonsei.ac.kr (T.-K. Hong).

http://dx.doi.org/10.1016/j.pepi.2015.05.009
0031-9201/

mainly for the vicinity around main-shock faults (e.g., Stein (1999) and Ma et al. (2005)). The regional seismicity changes for static stress changes have been poorly understood. Megathrusts produce lithospheric displacements in intraplate regions at a couple of thousand kilometers away, causing mild static stress changes that trigger earthquakes in regions of long-lived stress concentration (Hough et al., 2003; Jiang et al., 2010). The stress changes by megathrust is crucial for intraplate seismic hazards. The Korean Peninsula is located at a stable intraplate region, and is monitored by dense seismic networks. The environments provide a unique opportunity to investigate the temporal evolution of long-term intraplate seismicity after megathrust. In this study, we investigate the properties of seismicity in regional intraplate regions after megathrust.

2. Tectonic setting and data

The Korean Peninsula is placed in the far-eastern Eurasian plate that belongs to a stable intraplate region with a low earthquake occurrence rate and diffused seismicity (Houng and Hong, 2013). The Korean peninsula and the Yellow Sea display typical continental crusts, while the East Sea (Sea of Japan) presents a transitional structure between continental and oceanic crusts (Chough et al., 2000; Hong et al., 2008; Hong and Kang, 2009; Hong, 2010; He and Hong, 2010; Jo and Hong, 2013). The lithosphere around the peninsula is under influence of compressional stress field that is induced by collisions of Eurasian plate with neighboring plates (Pacific, Philippine Sea, and Indian plates). The composite tectonic-loading stress builds an ambient stress field with ENE-directional compression and SSE-directional tension (Choi et al., 2012) (Fig. 1).

The 11 March 2011 M9.0 Tohoku-Oki earthquake occurred in a region off the northeast coast of Japanese island on the boundary between the Pacific plate and the Okhotsk plate. The rupture plane of the Tohoku-Oki earthquake ha a dimension of ~440 km along the plate boundary and ~180 km along the slab interface (e.g., Yagi and Fukahata (2011)). The peak slip amount reaches ~50 m, and the vertical displacements around the epicenter range

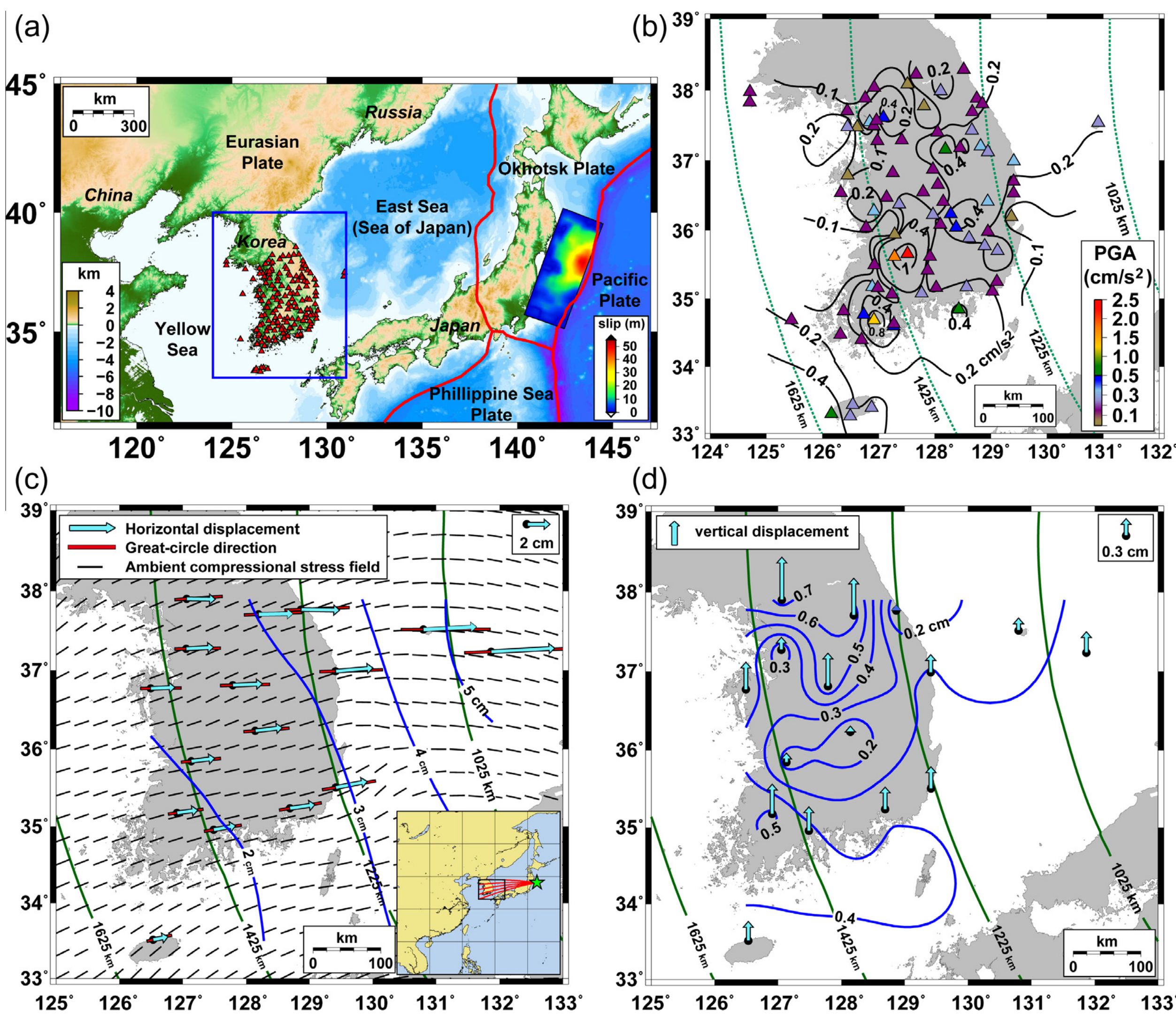

Fig. 1. (a) Tectonic structures around the 2011 Tohoku-Oki earthquake and the Korean Peninsula. The study area is marked with a blue rectangle. Seismic stations in the Korean Peninsula are marked with red triangles, and the plate boundaries with red solid lines. A source slip model for the Tohoku-Oki earthquake is presented on the epicentral area (Yagi and Fukahata, 2011). (b) Peak ground accelerations (PGAs) on the Korean Peninsula by the Tohoku-Oki earthquake. The PGAs in most regions are 0.1–0.4 cm/s^2. Localized large PGAs are observed. (c) Lateral lithospheric displacements by the 2011 Tohoku-Oki earthquake. The lateral displacement directions (cyan arrows) coincide with the great-circle directions (red bars) to the epicenter. The ambient compressional stress field is presented with broken lines. The epicentral distances are marked with green solid lines. The lateral displacements are inversely proportional to the epicentral distances. (d) Vertical displacements by the Tohoku-Oki earthquake. The vertical displacements are much smaller than the lateral displacements. (For interpretation of the references to color in this figure legend, the reader is referred to the web version of this article.)

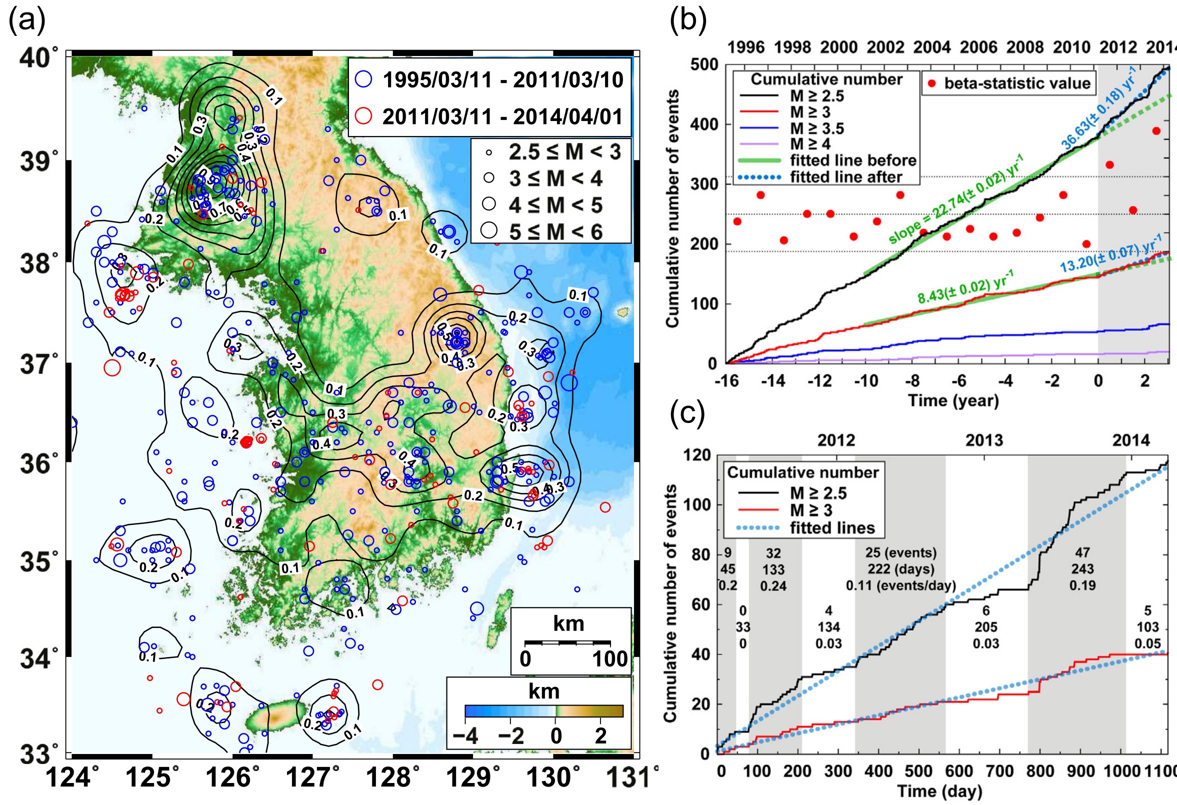

Fig. 2. (a) Comparison of seismicity before and after the great earthquake (blue dots for seismicity during 1995–2011, and red dots for seismicity during 2011–2014). The instrumental seismicity densities are presented in contours. (b) Temporal evolutions of cumulative numbers of earthquakes with magnitudes greater than 2.5, 3.0, 3.5 and 4.0 since 1995. The cumulative number of events increases with a constant rate until the occurrence of the 2011 Tohoku-Oki earthquake. The earthquake occurrence rate changes higher after the great earthquake. The average earthquake occurrence rates before and after the great earthquake are denoted. The beta-statistic values (red dots) are greater than 2 in the first and third years after the Tohoku-Oki earthquake. (c) An enlarged view of cumulative numbers of earthquakes ($M \geqslant 2.5$, 3.0) after the great earthquake. Characteristic episodic increases of seismicity (shaded time periods) are followed by seismically quiescent periods (white time periods). (For interpretation of the references to color in this figure legend, the reader is referred to the web version of this article.)

between −5.3 and 14.3 m (Yagi and Fukahata, 2011; Keliang and Jin, 2011). The Korean Peninsula is located at ~1300 km in the west from the epicenter of the 11 March 2011 M9.0 Tohoku-Oki earthquake (Fig. 1).

Strong ground motions with peak ground accelerations (PGAs) are 0.1–0.4 cm/s^2 are observed in the peninsula. The peak ground acceleration reaches 2.33 cm/s^2 in the southwestern peninsula. The lithosphere around the peninsula was dislocated by 1–6 cm in the direction to the epicenter, and was uplifted by 0.2–0.8 cm (Kim and Bae, 2012; Zhao et al., 2012) (Fig. 1(c) and (d)). The lithospheric dislocations are dominated by lateral (horizontal) movements. The horizontal dislocations are inversely proportional to the epicentral distances. The locations with horizontal dislocations of 5, 3 and 2 cm are placed approximately at epicentral distances of 1025, 1225 and 1425 km, respectively. The horizontal displacement directions are subparallel with the great-circle directions to the epicenter, suggesting that the lithospheric dislocations are associated with the Tohoku-Oki earthquake (Fig. 1(c)).

Dense seismic networks are deployed over the peninsula, allowing complete recording of seismic events with magnitudes greater than 2.5 since 1978 (Houng and Hong, 2013). Seismic data for earthquakes since 1996 are analyzed in this study (Fig. 2). The number of earthquakes up to 2014 after the Tohoku-Oki earthquake is 249. Seismic waveforms are collected from 182 stations (Fig. 1(a)). Focal mechanism solutions for earthquakes before the Tohoku-Oki earthquake are collected from various resources (Jun, 1991; Cipar, 1996; Park et al., 2007; Choi et al., 2012; Hong and Choi, 2012).

3. Methods

The strength of seismicity change is determined by Matthews and Reasenberg (1988):

$$\beta = \frac{n(t) - \bar{n}}{Std(n)}, \tag{1}$$

where n is the number of events at time t, $\bar{n}$ is the average number of events, and $Std(n)$ is the standard deviation of $n(t)$. The occurrence of earthquakes satisfies the Gutenberg–Richter frequency–magnitude relationship that is given by (e.g., Tinti and Mulargia (1985))

$$\log N = a - b \cdot M, \tag{2}$$

where M is the magnitude, N is the number of earthquakes with magnitudes greater than or equal to M, and a and b are constants. The Gutenberg–Richter frequency–magnitude relationship is determined by the maximum likelihood estimation (MLE) (Wiemer and Wyss, 2000).

The Coulomb stress change by an earthquake, ΔCFS, is given by (e.g., Harris (1998))

$$\Delta\mathrm{CFS} = \Delta\tau - \mu(\Delta\sigma_n - \Delta p), \tag{3}$$

where $\Delta\tau$ is the shear stress change, μ is the friction coefficient, $\Delta\sigma_n$ is the normal stress change (positive for increased compression), and Δp is the pore fluid pressure change. The friction coefficient

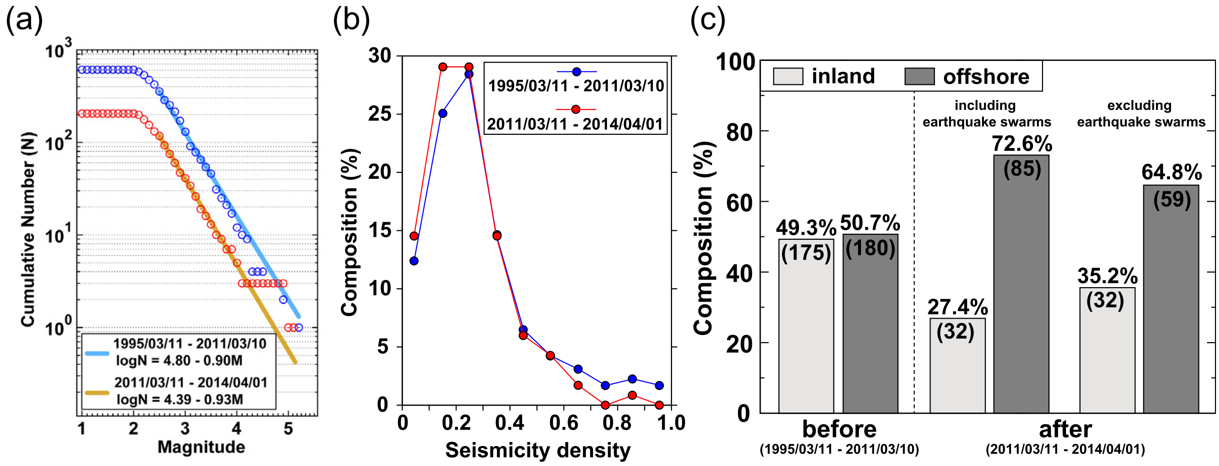

Fig. 3. (a) Comparison of the Gutenberg–Richter frequency–magnitude relationship before and after the great earthquake. The estimated b values are similar (0.90, 0.93). (b) Distribution of events as function of seismicity density. Events occur dominantly in the regions of mild seismicity densities (<0.3). (c) Comparison of earthquake composition before and after the Tohoku-Oki earthquake for events with magnitudes $M \geqslant 2.5$. An apparent concentration of seismicity in offshore regions is observed after the Tohoku-Oki earthquake.

changes with the pore pressure. Thus, the Coulomb stress change can be rewritten by Lin and Stein (2004) and Toda et al. (2005)

$$\Delta CFS = \Delta\tau - \mu'\Delta\sigma_n, \quad (4)$$

where μ' is the effective friction coefficient that is given by

$$\mu' = \mu(1 - B). \quad (5)$$

Here, B is the Skempton's coefficient that describes the pore pressure response to the mean stress under undrained conditions, varying between 0 and 1 (King et al., 1994). The differential lateral displacements build a tensional stress field ($\Delta\sigma_n < 0$), and make the pore fluid pressure increased ($\Delta p > 0$).

The radial strain, ϵ, induced by spatial differences in lithospheric dislocations is calculated by

$$\epsilon(i,j) = \frac{\Delta l_i^j}{l_i^j} = \frac{d_i^j - d_{i-1}^j}{r_i^j - r_{i-1}^j}, \quad (6)$$

where l_i^j is the reference distance to location i along path j, Δl_i^j is the differential lithospheric displacement, r_i is the epicentral distance of region i from the event, and d_i^j is the lithospheric displacement at location i along the direction j. The induced tensional stress is given by

$$\sigma = E\epsilon, \quad (7)$$

where E is the Young's modulus for elastic material,

$$E = \frac{(3\lambda + 2\xi)\xi}{(\lambda + \xi)}. \quad (8)$$

Here λ and ξ are the Lamé constants satisfy

$$\lambda = \rho V_P^2 - 2\rho V_S^2, \quad \xi = \rho V_S^2, \quad (9)$$

where ρ is the density of material, V_P is the P velocity, and V_S is the S velocity.

The hypocentral parameters of events are refined using the P and S arrival times (Klein, 2007). The hypocenters of clustered events are determined using a double difference location algorithm (Waldhauser and Ellsworth, 2000). A reference focal depth for the double difference relocation is determined considering the distribution of focal depths from a conventional traveltime-based hypocentral inversion method. An 1-D crustal velocity model (Chang and Baag, 2006) is implemented for the hypocentral-parameter inversion.

The focal mechanism solutions are calculated using polarity analyses for small earthquakes and low-frequency waveform inversions for moderate-size earthquakes. The polarity analysis is based on the first-arrival P polarities (Hardebeck and Shearer, 2002, 2003). The focal depths and magnitudes are determined from the low-frequency waveform inversion (Dreger and Helmberger, 1990; Hong and Rhie, 2009). The Green's functions for the structures between events and stations are calculated based on a global-averaged 1-D velocity model (Kennett et al., 1995) that is appropriate for low frequency waves (Saikia, 1994). A set of hypocentral parameters yielding best-fit synthetic waveforms is selected. The similarity between observed and synthetic waveforms is quantified in terms of variance reduction, R:

$$R = \left[1.0 - \frac{\int |o(t) - s(t)|^2\,dt}{\int o(t)^2\,dt}\right] \times 100, \quad (10)$$

where $o(t)$ is the observed waveform at time t, and $s(t)$ is the synthetic waveform.

4. Coulomb stress change and induced tension field

The regional Coulomb stress change (ΔCFS) by the 2011 Tohoku-Oki earthquake is calculated from Eq. (3) with the lithospheric Young's modulus of 80 GPa and Poisson's ratio of 0.25 (King et al., 1994; Harris, 1998; Lin and Stein, 2004; Toda et al., 2005; Yagi and Fukahata, 2011). The effective friction coefficient (μ') is set to be 0.4 that is widely accepted for subduction zones (e.g., Nalbant (1998), Ma et al. (2005), Toda et al. (2005), Freed et al. (2007), Toda and Enescu (2011), and Catalli and Chan (2012)). The ambient regional stress field around the Korean Peninsula is N75°E-directional compression (Fig. 1(c); Choi et al. (2012)). The magnitude of the regional stress field is set to be 65 bars (Junn et al., 2002). The optimal orientations of faults are calculated considering the ambient regional stress field and earthquake-inducing stress (Fig. 4).

The Coulomb stress changes for optimally-oriented faults are presented in Fig. 4. The optimal fault-plane directions are close to the observed fault-plane solutions of earthquakes before the megathrust (Fig. 4(d)). Strike-slip earthquakes are most dominant, and normal-faulting earthquakes are populated in the central Yellow Sea and northwest coast of peninsula (region C in Fig. 4(d)). Thrust events are clustered in the region off the east

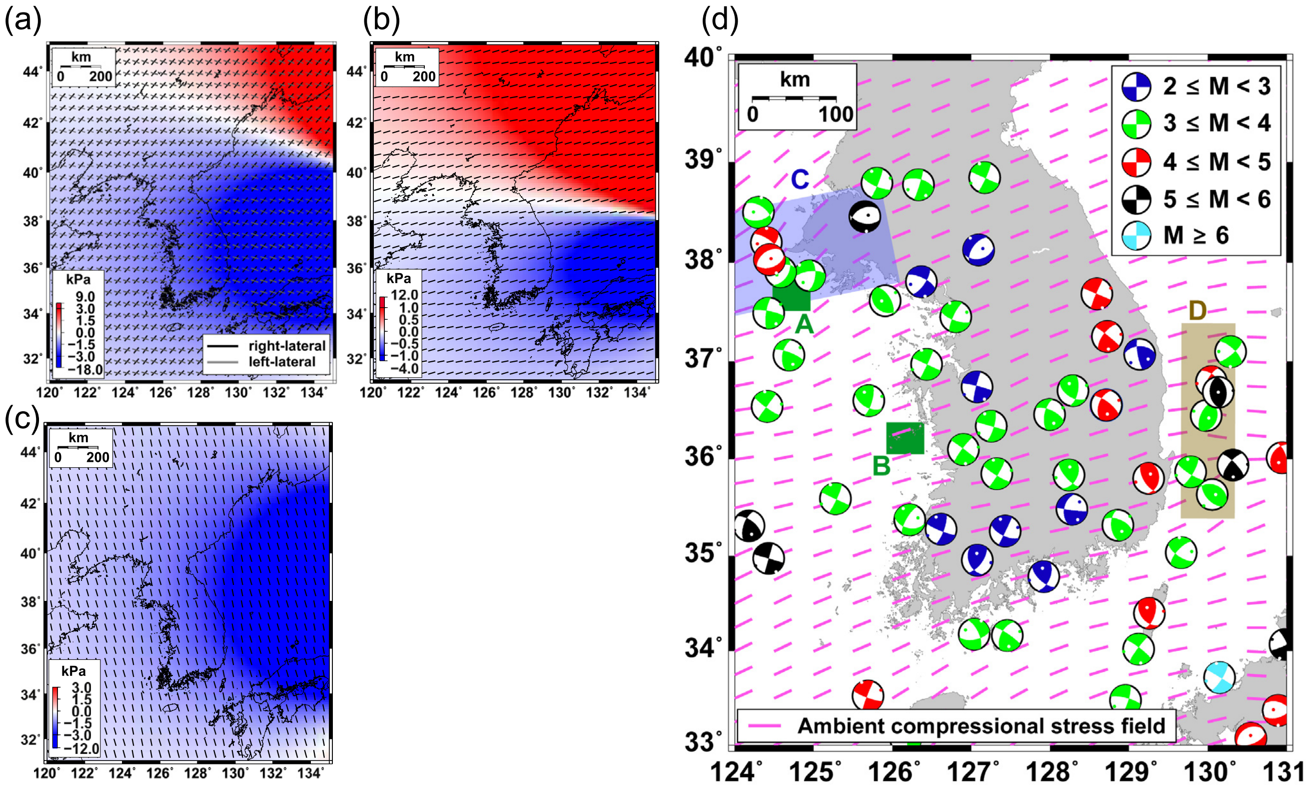

Fig. 4. The Coulomb failure stress changes by the 2011 Tohoku-Oki earthquake for optimally-oriented (a) strike-slip, (b) normal, and (c) thrust faults. The rupture trace on the surface is marked with a thick green line. The fault-plane directions of optimally-oriented faults are presented with thick black and gray lines. Positive Coulomb stress changes are observed around the Korean Peninsula for optimally-oriented strike-slip and normal faults, while negative Coulomb stress changes for optimally-oriented thrust faults. (d) Focal mechanism solutions of earthquakes before the Tohoku-Oki earthquake. The ambient compressional stress field is presented with dotted lines. Regions A and B are the locations of earthquake swarms observed after the Tohoku-Oki earthquake. Strike-slip earthquakes are dominant around the peninsula. Normal-faulting earthquakes are populated in region C, and reverse-faulting earthquakes are observed in region D. (For interpretation of the references to color in this figure legend, the reader is referred to the web version of this article.)

coast of the peninsula (region D). It is observed that the megathrust builds negative Coulomb stress changes for all types of faults around the Korean Peninsula, constructing stress shadows (Fig. 4). The Coulomb stress changes reach -3.0 kPa for optimally-oriented strike-slip and thrust faults, and -1.0 kPa for optimally-oriented normal faults around the southern Korean Peninsula.

A horizontal displacement field discretized by 0.05°-by-0.05° cells is constructed by interpolating the geodetic data. Differential dislocations along the great-circle paths are calculated at every 0.1° in latitude and longitude from the horizontal displacement field. An interpolated differential dislocation field is constructed from the differential dislocations. The radial strains induced by the coseismic lithospheric dislocation are estimated at every 20 km along the great-circle paths from the megathrust. The radial strains are translated into radial stresses using Eq. (6) (Fig. 5). The focal depths of the earthquakes are 5–15 km, suggesting the event occurrence in mid-crust. The Young's modulus for the mid-crust is determined to be 68 GPa from Eq. (8) with the P velocity (V_P) of 5.8 km/s, S velocity (V_S) of 3.2 km/s, and density (ρ) of 2.6 g/cm^3.

The differential lateral displacements produce tensional strains of $\sim 1 \times 10^{-7}$ in the East Sea, 0.3×10^{-7} to 0.8×10^{-7} in the inland peninsula, and $\sim 0.3 \times 10^{-7}$ in the Yellow Sea (Fig. 5). The equivalent lateral tensions are 1–7 kPa in the mid-crust (Fig. 5). The induced tensions are consistent with the calculated Coulomb stress changes. These induced stress changes are comparable to those observed in remote triggering, which are in the order of a few kPa to a few MPa depending on local conditions (Brodsky and Prejean, 2005; Gomberg et al., 2001; Miyazawa, 2011; Wu et al., 2014). The negative Coulomb stress changes and induced tensional stress field build stress shadows, making the medium relaxed. The ambient stress field before the megathrust is expected to be recovered gradually by tectonic loading, requiring interseismic strain accumulation (Simpson et al., 1988; Jaumé and Sykes, 1996; Harris, 1998).

5. Seismic velocity change

The coseismic deformation in the media accompanies seismic velocity changes (e.g., Brenguier et al. (2008)). The seismic velocities in the crust before and after the megathrust are inferred from the traveltimes of seismic phases of two doublet events that occurred in the region off the east coast of Japanese islands (Fig. 6). One event (E1) occurred in September 30, 2010, and the other event (E2) occurred in August 21, 2011. The two events are separated by 0.634 km, and the fault-plane solutions are very close. The magnitudes of the events are M_W4.9 and 4.6. Three station pairs (DGY-GAHB, ULLB-SEO, CHJ-SES) are selected. The epicentral distances are 906–1306 km. The inter-station distances are 136, 196, and 353 km.

The vertical seismic waveforms are bandpass-filtered between 0.07 Hz (or 0.05 Hz) and 0.1 Hz considering the frequency contents. The waveform records are aligned for the onset times of P waves. The doublet events display high similarity in waveforms (Fig. 6). The S arrival-time differences are smaller (*le*0.1 s) than P arrival-time differences at all stations. We find systematic traveltime differences in the fundamental-mode Rayleigh waves, Rg.

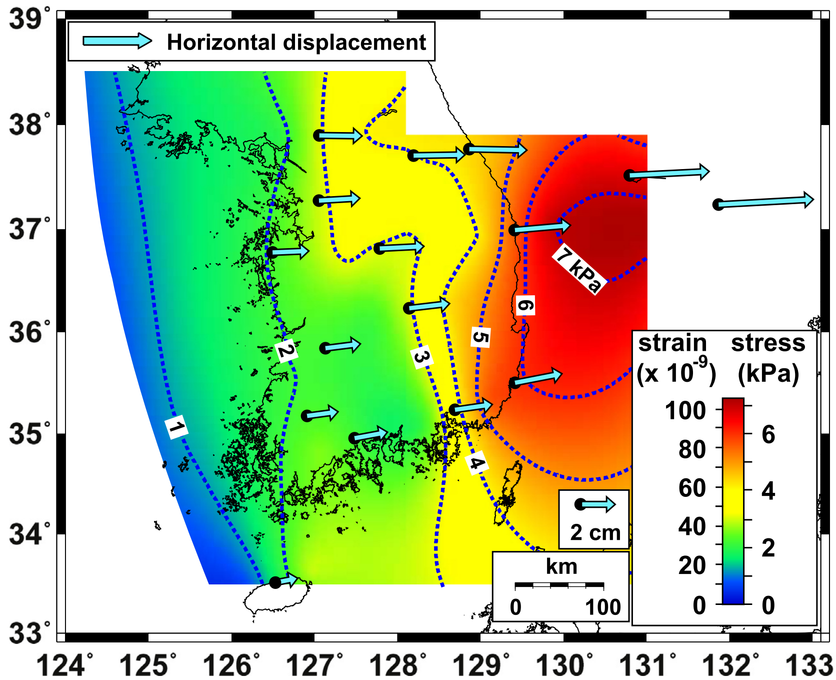

Fig. 5. The tensional strains and stresses induced by the spatial variations of lateral displacements. The tensional stresses are effective in the great-circle directions to the epicenter of the Tohoku-Oki earthquake. The tensional stresses are greater than 6 kPa in the East Sea region, and are less than 2 kPa in the Yellow Sea region. (For interpretation of the references to color in this figure legend, the reader is referred to the web version of this article.)

The eastern stations (DGY, ULLB, CHJ) present *Rg* traveltime differences less than 0.1 s, while the western stations (GAHB, SEO, SES) have larger *Rg* traveltimes differences of 0.70–0.79 s. The double-difference *Rg* traveltimes between stations on common great-circle directions are 0.81 s for the northern path, 0.74 s for the central path, and 0.69 s for the southern path. The *S*-wave traveltimes change little, while the *Rg* traveltimes increase noticeably after the megathrust. The *Rg* waves are preferentially influenced by crustal properties, while the *S* waves are affected by upper-mantle properties. These observations suggest seismic velocity decreases in the crust, supporting the medium relaxation by the tension induced by the megathrust.

6. Temporal changes of seismicity properties

The temporal variations of beta-statistic values, earthquake occurrence rates, and cumulative numbers of earthquakes are compared before and after the megathrust (Fig. 2(b)). The cumulative numbers of events with $M \geqslant 2.5$, 3.0, 3.5 and 4.0 are calculated. The temporal variations of cumulative numbers of earthquakes are fitted with least-squares lines. We find apparent increases of earthquakes after the megathrust (Fig. 2(b)). The annual occurrence rates of earthquakes with $M \geqslant 2.5$ are 22.87 times per year for the period before the megathrust, and 36.63 times per year (about 61.1% increase) for the period after the megathrust. Also, the annual occurrence rates for earthquakes with magnitudes greater than 3.0 are 8.43 times per year for the period before the megathrust, and 13.20 times per year (about 56.6% increase) for the period after the megathrust (Fig. 2(b)).

The apparent seismicity increase after megathrust is not in accord with the observed stress shadows in which the seismicity is expected to decrease (e.g., Harris (1998)). It is also intriguing to note that the cumulative numbers of earthquakes after the megathrust increase intermittently, suggesting episodic occurrence of earthquakes (Fig. 2(c)). We observe that time durations of active seismicity are comparable to those of the following seismic quiescence. The seismicity increases abruptly in the first year after the megathrust, which is followed by an aseismic period in the second year. Earthquake swarms are observed in the third year at two localized regions of the Yellow Sea.

The magnitude-dependent earthquake occurrence rates are estimated in terms of *b* values of the Gutenberg–Richter frequency–magnitude relationship (Fig. 3). The magnitude-dependent earthquake occurrence rates (*b*) are 0.90 for 16 years before the megathrust (11 March 1995–10 March 2011), and 0.93 for 3 years after the megathrust (11 March 2011–1 April 2014) (Fig. 3(a)). The increased seismicity with similar *b* values suggests that the medium properties may be kept constant after the megathrust, and the postseismic stress environment may be much favorable for yielding earthquakes. The distribution of postseismic events generally agree with the spatial seismicity densities before the megathrust. Seismic events appear to be concentrated in mild seismicity-density regions with the normalized seismic densities less than 0.3 (Fig. 3(b)). The post-megathrust seismicity is populated in offshore regions, which is apparent even with the seismicity excluding the earthquake swarms in Yellow Sea (Fig. 3(c)).

7. Temporal concentration of moderate-size earthquakes

Seven earthquakes with $M_L \geqslant 4.9$ occurred around the Korean Peninsula since 1978 until the occurrence of the Tohoku-Oki earthquake. Only one earthquake out of the seven earthquakes occurred in the Yellow Sea region. It was reported that moderate-size or larger earthquakes are generally suppressed in stress shadows for several years to decades (Jaumé and Sykes, 1996; Harris, 1998). We, however, observe three earthquakes with $M_L \geqslant 4.9$ in the Yellow Sea region for one year from April 2013 to April 2014 in two years after the Tohoku-Oki earthquake (Fig. 7(a)). These earthquakes are the largest events since the 29 May 2004 M5.2 earthquake. Further, it is unusual to observe such moderate-size

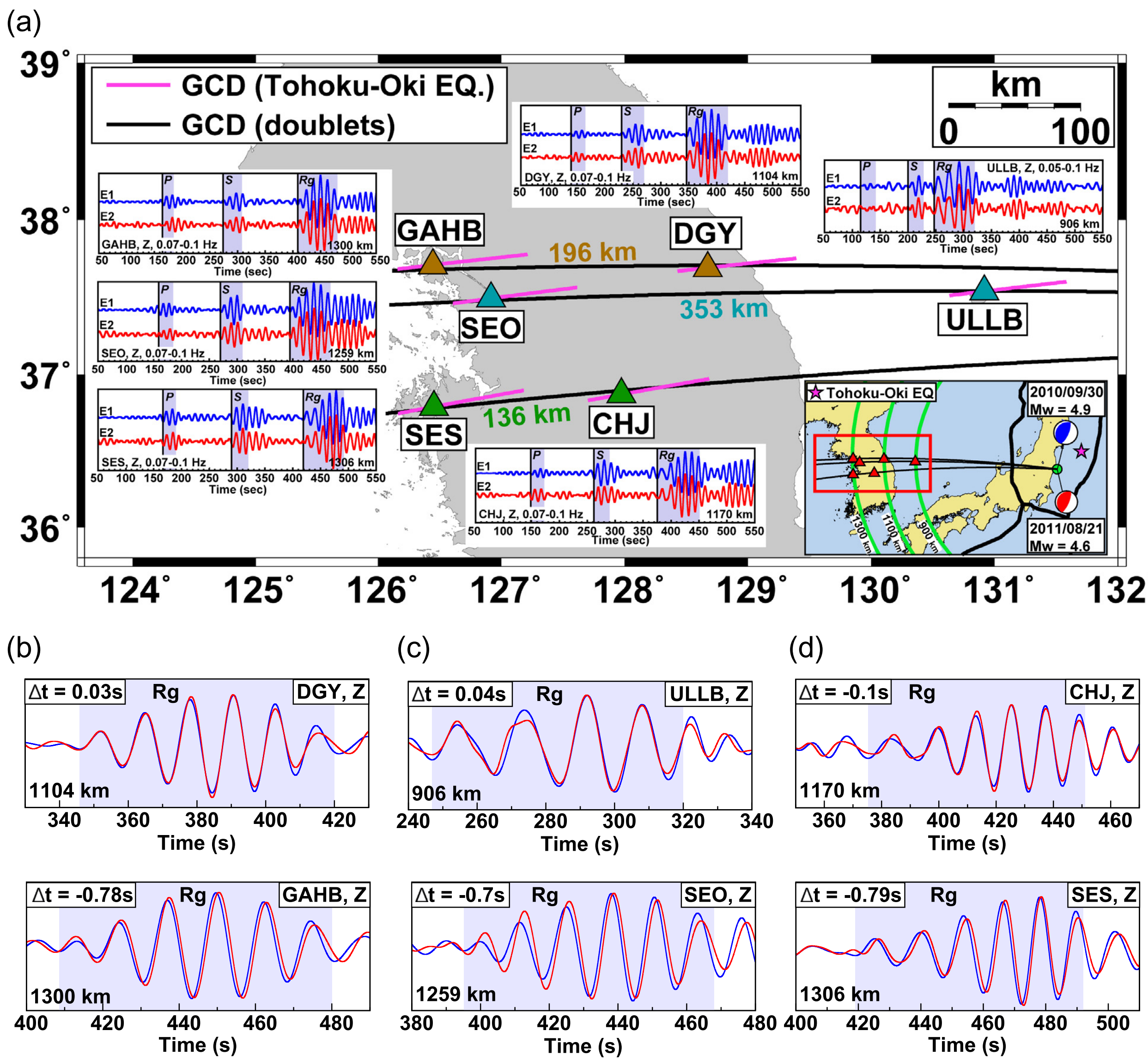

Fig. 6. Analysis of traveltimes of seismic waves from doublet events off the east coast of the Japanese islands. (a) Map of the doublets and stations analyzed. The doublet waveforms at the stations are presented on the map. Inter-station distances are denoted. The great-circle directions for the doublets and those for the Tohoku-Oki earthquake are presented. Enlarged *Rg* waveforms for three station pairs: (b) DGY-GAHB pair (northern great-circle path), (c) ULLB-SEO pair (central path), and (d) CHJ-SES pair (southern path). The traveltime differences at the eastern stations are less than 0.1 s, while those at the western stations are 0.7–0.79 s.

events to be populated in the Yellow Sea region during a short-time period.

A long-period waveform inversion method is applied for the determination of focal mechanism solutions of 6 moderate-size events with magnitudes greater than 3.3, and a seismic-polarity analysis is used for the focal mechanism solutions of 28 small-size events. Waveforms from 6 to 7 stations are combined for the long-period waveform inversions. The long-period waveform inversion is based on 200-s-long waveform record sections in frequencies of 0.05–0.1 Hz. The best-fit focal depth is searched from 1 to 20 km. The focal mechanism solutions of earthquakes before the megathrust are collected from early studies for comparison with those after the megathrust (Jun, 1991; Cipar, 1996; Park et al., 2007; Choi et al., 2012; Hong and Choi, 2012; Fig. 7).

The three moderate-size earthquakes are observed to be strike-slip events with fault-plane directions of 197°–228° (or, equivalently 287°–310°). The focal depths are determined to be 5–10 km, which correspond to upper crust (Fig. 7). The focal mechanism solutions are close to those observed before the megathrust (Choi et al., 2012; Hong and Choi, 2012). The consistent focal mechanism solutions imply that the post-megathrust earthquakes occur in a similar stress environment. However, the abrupt increase of moderate-size earthquakes during a short-time period suggests a decrease of critical shear stress for faulting, which may be a consequence of pore-fluid pressure increase in the medium.

8. Earthquake swarms

Earthquake swarms are observed in two regions of the Yellow Sea (regions A and B in Fig. 7(a)), which is unusual in stable intraplate region. The earthquake swarm in region A is composed of 45 earthquakes during 29 April 2013–10 November 2013. The magnitudes of events are 0.7–4.9. Another earthquake swarm was observed in region B in which 108 earthquakes with magnitudes of 0.7–3.5 occurred during 3 June 2013–14 September 2013. It is noteworthy that earthquakes with magnitudes of $M_L \geqslant 2.0$ were rarely observed in regions A and B before the megathrust.

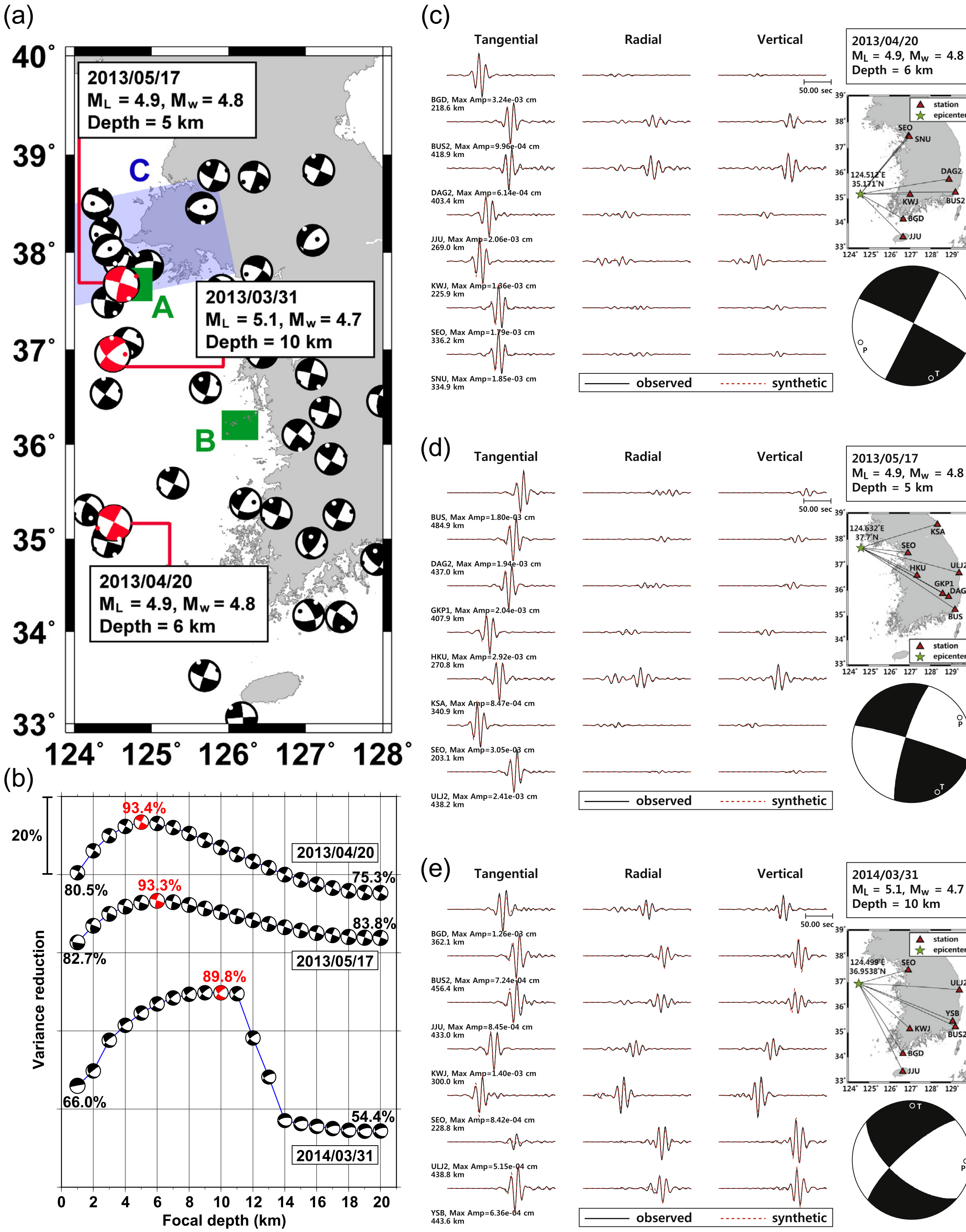

Fig. 7. (a) Focal mechanism solutions of moderate-size earthquakes with magnitudes of 4.9–5.1 (red beachballs) around the Korean Peninsula after the Tohoku-Oki earthquake. The focal mechanism solutions for events before the Tohoku-Oki earthquake are presented with black beachballs. Earthquake swarms developed in regions A and B. The paleo-continental-collision region with normal-faulting events is shaded (region C). The *P*-axis directions are consistent with the ambient stress field. (b) Determination of focal depths from the variance reduction analysis. The focal depths are determined to be 5–10 km. Long-period waveform inversions of (c) the 20 April 2013 M_L4.9 earthquake, (d) the 17 May 2013 M_L4.9 earthquake, and (e) the 31 March 2014 M_L5.1 earthquake for the best-fit focal depths. (For interpretation of the references to color in this figure legend, the reader is referred to the web version of this article.)

We collect 194 *P* arrival times and 32 *S* arrival times from 10 local and regional stations for the events in region A. Also, 1040 *P* arrival times and 756 *S* arrival times are collected from 30 stations for the events in region B. The *P* and *S* arrival times are determined using waveform cross-correlation. The *P* and *S* waves are searched in time windows between −0.5 and 3.0 s and between −0.5 and 7.0 s with respect to the theoretical arrival times. The numbers of *P* and *S* waves are 1040 and 756, which produces

11,984 pairs of *P* and *S* arrival times with cross-correlation coefficients greater than 0.6. The hypocenters of the events in regions A (45 events) and B (108 events) are initially determined using a conventional traveltime-based hypocentral inversion method (Klein, 2007). We further refine the hypocentral parameters of 96 clustered events among 108 events in region B using a double-difference location method (Waldhauser and Ellsworth, 2000).

The earthquakes in region A are clustered in an NE-directional 20 km-by-10 km area (Fig. 8). The earthquake swarm includes an M4.9 earthquake. Region A is placed around the southern margin of region C that may correspond to the paleo-collision boundary between the North and South China blocks (Hong and Choi, 2012). Normal-faulting earthquakes are dominant in region C (Hong and Choi, 2012). However, the earthquakes are observed to be strike-slip events with fault-plane strikes of ~17° (alternatively, ~107°). The resolved fault-plane strikes are different from the apparent spatial distribution of earthquakes that directs to ~60°. This direction is approximately subparallel with the fault-plane strikes of normal-faulting events in region C (~70.3° ± 10.3°). The observation suggests that a series of subparallel strike-slip faults may be developed in the crust of region A as a consequence of coseismic stress.

The earthquakes in region B are distributed over a ~2.5-km-long NE-directional region (Fig. 9). The waveform similarity supports the clustering of earthquakes in a small area (Fig. 10). The events bifurcate at the northeastern area in region B. The focal depths are 9–11 km (Fig. 9(d)). The focal mechanism solutions suggest strike-slip earthquakes with fault strikes in 18°–59°. The compression-axis directions of the focal-mechanism solutions are consistent with the ambient stress field (Choi et al., 2012; Hong and Choi, 2012). The earthquakes are populated in three active-seismic periods, i.e., periods I, III, and V in Fig. 9(c). It is observed that 92 events out of 108 events (~85%) occurred during active-seismic periods (37 days).

The earthquake swarm in region B presents characteristic migrations. The earthquakes migrate in SW with a speed of 1.16 m/h during period I, and in NE with a speed of 3.57 m/h during period III. Another set of earthquakes occur progressively in NNE during period V from the origin of the earthquake swarm of period I, depicting splay faults. These temporal migrations of events suggest slow successive ruptures. The earthquakes are populated at depths of 9–10 km during periods I and III, and 10–11 km during period V. The focal depths present linear variations with time.

The observed migration speeds and focal depths are consistent with those of earthquake swarms in fluid-saturated environment (Hariri et al., 2010). The fluids such as water and hydrocarbons are reported to be abundant in the crust (Fyfe et al., 1978; Piombo et al., 2005). In particular, the water is the most abundant among fluids, and is present in the mid-crust (Kerr, 1993, 1994). The presence of fluids supports the occurrence of earthquakes swarms in the mid-crust. The earthquake swarm in region B suggests successive faulting of intact media, which may be a consequence of temporal increase of pore-fluid pressure (Hickman et al., 1995; Hariri et al., 2010; Brodsky and van der Elst, 2014).

9. A model of earthquake occurrence in stress shadows

Negative Coulomb stress changes were expected for all types of faults around the southern Korean Peninsula after the Tohoku-Oki

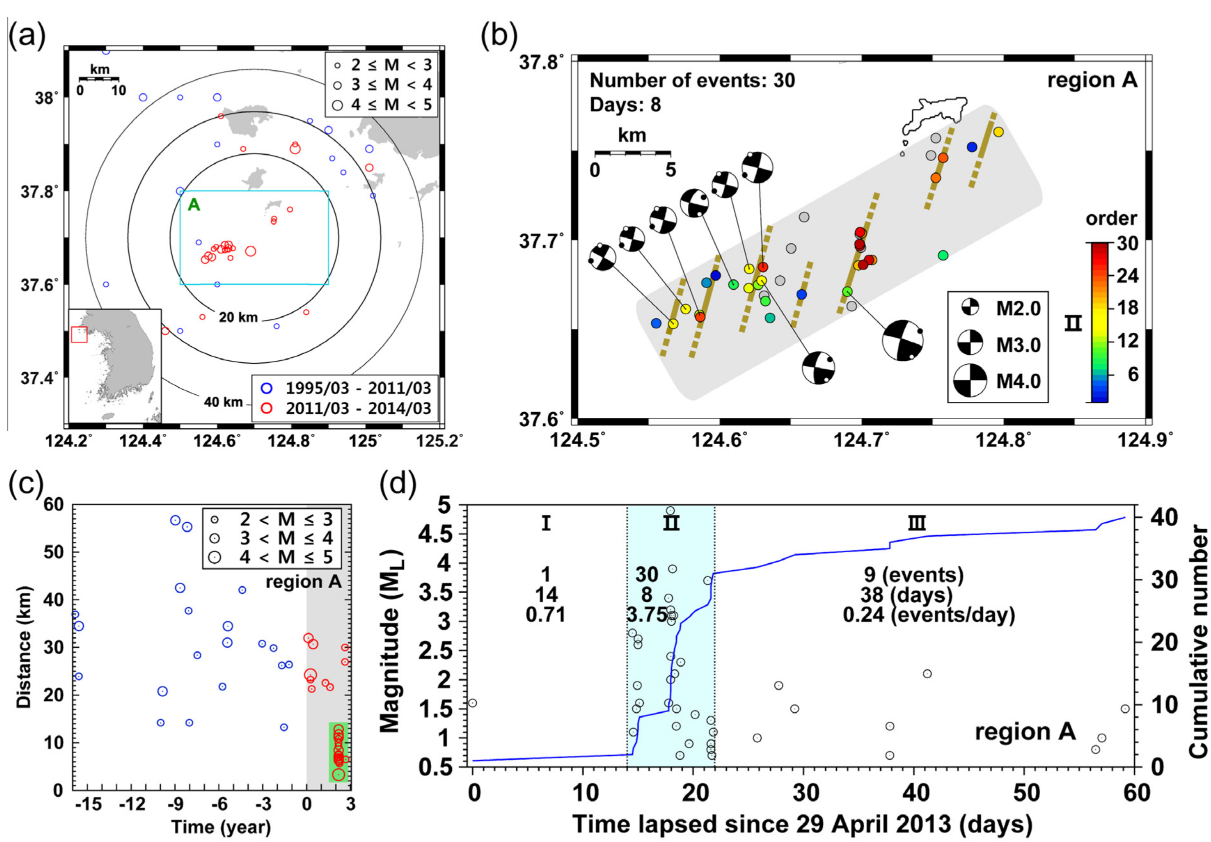

Fig. 8. (a) Seismicity around region A. (b) Epicentral distribution and focal mechanism solutions of earthquakes. The events display NE-directional distribution, while the fault planes strike in NNE. (c) Temporal variation of distances from events to the central location of region A. Earthquakes rarely occurred in region A before the Tohoku-Oki earthquake. (d) Temporal distribution of earthquakes in region A. The earthquakes are populated in period II.

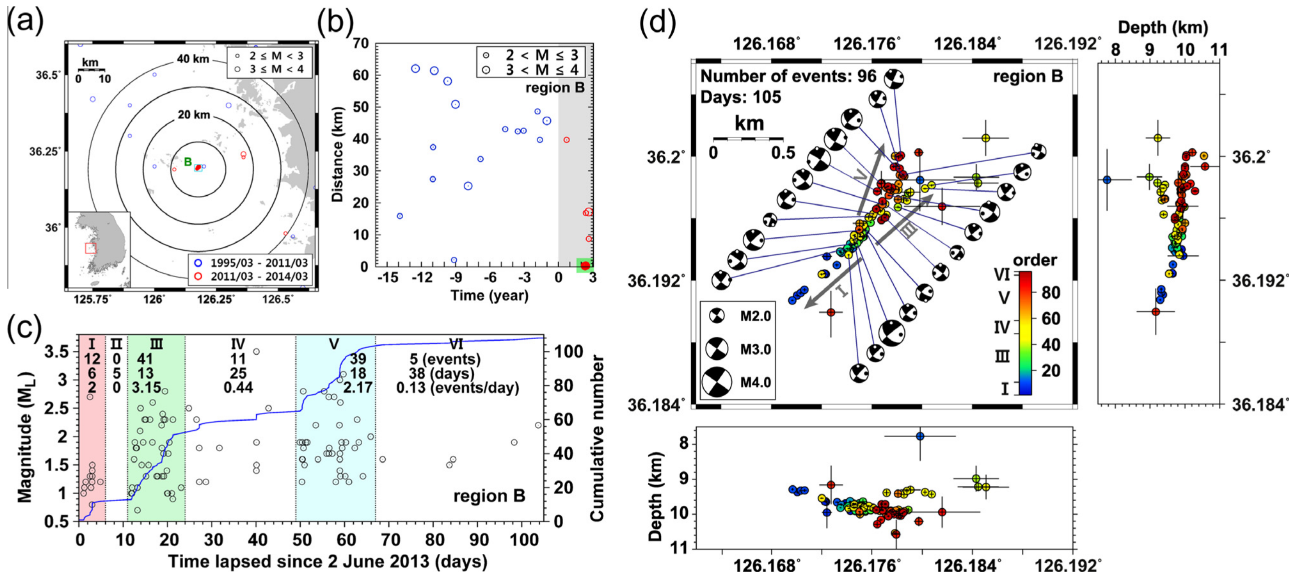

Fig. 9. (a) Seismicity around region B. The epicenters of events before (blue circles) and after the Tohoku-Oki earthquake (red circles) are presented. (b) Temporal variation of distances from events to the central location of region B. Earthquake rarely occurred in region B. (c) Temporal distribution of earthquakes in region B. Events are populated in periods I, III and V. The event occurrence rates are presented. (d) The spatial distribution of earthquakes in region B, and the focal mechanism solutions. The event occurrence order is indicated in color. The events migrate in SW during period I, in NE during period III, and in NNE during period V. The focal depths increase generally with time. (For interpretation of the references to color in this figure legend, the reader is referred to the web version of this article.)

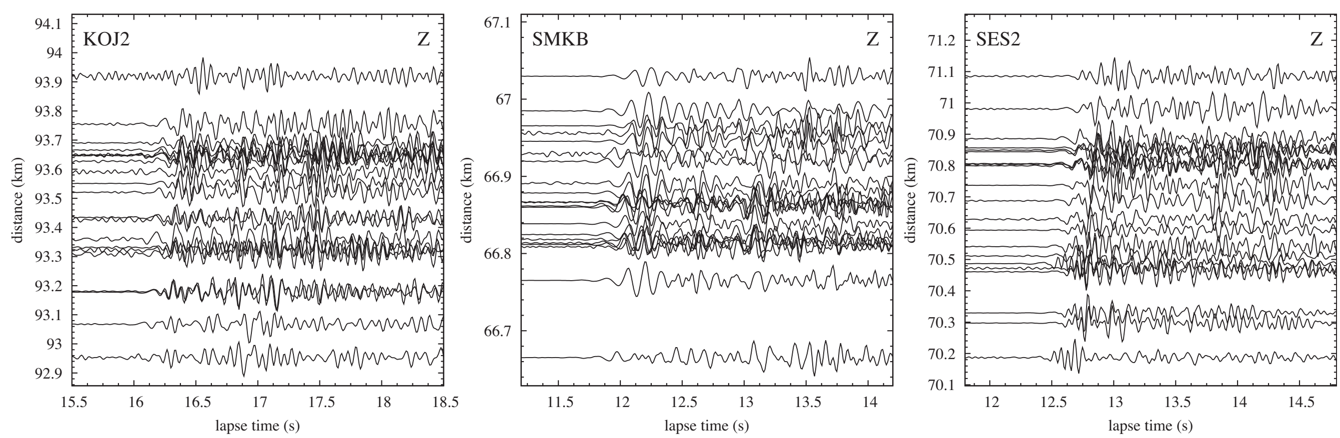

Fig. 10. Seismic waveforms for earthquakes in region B at three local stations. The event waveforms display high similarity.

earthquake, constructing stress shadows (Fig. 4). The differential lateral displacements and seismic velocity changes support the negative Coulomb stress changes (Figs. 5 and 6). However, the seismicity around the Korean Peninsula was observed to increase significantly after the megathrust, which is different from the expected seismicity decrease (Fig. 2). The increased seismicity is observed widely over the peninsula, and is populated in regions of moderate-seismicity densities. Also, the compression-axis directions are found to be consistent in the events before and after the megathrust. The observations suggest that the increased seismicity may be time-advanced events (Gomberg et al., 1997).

It is known that fluids (e.g., H_2O, CO_2, CH_4) are abundant in mid-crust (Kerr, 1993, 1994; Piombo et al., 2005). The fluids may be originated from the mineral dehydration during prograde metamorphism (Kerrich et al., 1984; Hickman et al., 1995). The fluids may be diffused in the crust during the coseismic differential dislocations that construct transient tension field (Scholz et al., 1973; Rice and Gu, 1983). As the ambient compressional stress field is recovered by tectonic loading (Harris, 1998), the fluids may migrate from regions of high compression to regions of low compression (Piombo et al., 2005). The fluids are confined in the pores, and resist to the ambient compressional stress that is gradually recovered.

The fluids in the pores hinder the increase of effective normal stress ($\sigma_n - P_f$ where σ_n is the normal stress and P_f is the pore-fluid pressure), while the shear stress keeps increasing with gradual recovery of ambient stress field. This situation constructs an environment with high shear stress and low effective normal stress, lowering the critical shear-stress levels required for faulting (e.g., Sibson (1985), Hickman et al. (1995), Fournier (1996), Felzer and Brodsky (2005), and Costain (2008)). Earthquakes may occur episodically on fault planes of which shear stresses are temporally greater than the effective normal stresses. This process may continue with incorporation of earthquake swarms until the lithostatic stresses are fully recovered.

10. Discussion and conclusions

A significant increase of seismicity with episodic occurrence of earthquakes was observed around the Korean Peninsula for several years after the 2011 Tohoku-Oki earthquake. The locations of post-megathrust earthquakes are generally consistent with the seismicity density before the megathrust. Also, unusual intensive occurrence of earthquake swarms and moderate-size earthquakes was observed. The intensive occurrence of moderate-size earthquakes may be a consequence of time advance of potential earthquakes in the region.

The megathrust produced strong transient waves with large lateral dislocations in local and regional distances. The differential lateral lithospheric dislocations built a transient radial tension field over wide backarc regions, constructing stress shadows for every type of fault in optimal orientation. The seismic-velocity decrease in the crust after the megathrust supports the medium relaxation by the coseismic lithospheric dislocation. Fluids may be diffused by the transient tension field, and may be confined in the pores. The characteristic seismicity increase and earthquake swarms in post-megathrust stress shadows may be ascribed to the decrease of effective normal stress by pore-fluid pressure increase (e.g., Toda and Stein (2003) and Talwani et al. (2007)). The induced seismicity may continue until the ambient stress field is fully recovered (Freed, 2005; Durand et al., 2010).

Acknowledgments

The Time-Domain Moment Tensor Inverse Code software package (Dreger, 2003) was used for long-period waveform inversion. Coulomb 3.3 software (Toda et al., 2011) was applied for the calculation of regional Coulomb stress changes. We thank Dr. Taka'aki Taira for fruitful discussion on seismic velocity changes after earthquakes. We are grateful to the Korea Meteorological Administration (KMA) and the Korea Institute of Geoscience and Mineral Resources (KIGAM) for seismic waveforms available. We thank the editor, Professor Vernon Cormier, and four anonymous reviewers for valuable comments. This work was supported by the Korea Meteorological Administration Research and Development Program under Grant KMIPA 2015-7040.

References

Brenguier, F., Campillo, M., Hadziioannou, C., Shapiro, N.M., Nadeau, R.M., Larose, E., 2008. Postseismic relaxation along the San Andreas Fault at Parkfield from continuous seismological observations. Science 321, 1478–1481.
Brodsky, E.E., Prejean, S.G., 2005. New constraints on mechanisms of remotely triggered seismicity at Long Valley Caldera. J. Geophys. Res. 110, B04302. http://dx.doi.org/10.1029/2004JB003211.
Brodsky, E.E., van der Elst, N.J., 2014. The uses of dynamic earthquake triggering. Annu. Rev. Earth Planet. Sci. 42, 317–339.
Catalli, F., Chan, C.-H., 2012. New insights into the application of the Coulomb model in real-time. Geophys. J. Int. 188, 583–599.
Chang, S.-J., Baag, C.-E., 2006. Crustal structure in Southern Korea from joint analysis of regional broadband waveforms and travel times. Bull. Seismol. Soc. Am. 96, 856–870.
Choi, H., Hong, T.-K., He, X., Baag, C.-E., 2012. Seismic evidence for reverse activation of a paleo-rifting system in the East Sea (Sea of Japan). Tectonophysics 572–573, 123–133.
Chough, S.K., Kwon, S.-T., Ree, J.-H., Choi, D.-K., 2000. Tectonic and sedimentary evolution of the Korean Peninsula: a review and new view. Earth Sci. Rev. 52, 175.
Cipar, J.J., 1996. Earthquake focal mechanisms in northeastern China and Korea determined by the grid search algorithm. Environmental Research Papers, no. 1997. Phillips Laboratory.
Costain, J.K., 2008. Intraplate seismicity, hydroseismicity, and predictions in hindsight. Seismol. Res. Lett. 79 (4), 578–589.
Dreger, D.S., 2003. TDMT INV: time domain seismic moment tensor INVersion. In Lee, W.H.K., Kanamori, H., Jennings, P.C., Kisslinger, C. (Eds.). International Handbook of Earthquake and Engineering Seismology. vol. B. pp. 1627.
Dreger, D.S., Helmberger, D.V., 1990. Broadband modeling of local earthquakes. Bull. Seismol. Soc. Am. 80, 1162–1179.
Durand, V., Bouchon, M., Karabulut, H., Marsan, D., Schmittbuhl, J., Bouin, M.P., Aktar, M., Daniel, G., 2010. Seismic interaction and delayed triggering along the North Anatolian Fault. Geophys. Res. Lett. 37, L18310. http://dx.doi.org/10.1029/2010GL044688.
Felzer, K.R., Brodsky, E.E., 2005. Testing the stress shadow hypothesis. J. Geophys. Res. 110, B05S09. http://dx.doi.org/10.1029/2004JB003277.
Fournier, R.O., 1996. Compressive and tensile failure at high fluid pressure where preexisting fractures have cohesive strength, with application to the San Andreas Fault. J. Geophys. Res. 101 (B11), 25499–25509.
Freed, A.M., 2005. Earthquake triggering by static, dynamic, and postseismic stress transfer. Annu. Rev. Earth Planet. Sci. 33, 335–367.
Freed, A.M., Lin, J., 2001. Delayed triggering of the 1999 Hector Mine earthquake by viscoelastic stress transfer. Nature 411, 180–183.
Freed, A.M., Ali, S.T., Burgmann, R., 2007. Evolution of stress in Southern California for the past 200 years from coseismic, postseismic and interseismic stress changes. Geophys. J. Int. 169, 1164–1179.
Fyfe, W.S., Price, N.J., Thomson, A.B., 1978. Fluids in the Earths Crust. Elsevier, Amsterdam.
Gomberg, J., Blanpied, M.L., Beeler, N.M., 1997. Transient triggering of near and distant earthquakes. Bull. Seismol. Soc. Am. 87 (2), 294–309.
Gomberg, J., Reasenberg, P.A., Bodin, P., Harris, R.A., 2001. Earthquake triggering by seismic waves following the Landers and Hector Mine earthquakes. Nature 411, 462–466.
Gonzalez-Huizar, H., Velasco, A.A., Peng, Z., Castro, R.R., 2012. Remote triggered seismicity caused by the 2011, M9.0 Tohoku-Oki, Japan earthquake. Geophys. Res. Lett. 39, L10302. http://dx.doi.org/10.1029/2012GL051015.
Hardebeck, J.L., Shearer, P.M., 2002. A new method for determining first-motion focal mechanisms. Bull. Seismol. Soc. Am. 92, 2264–2276.
Hardebeck, J.L., Shearer, P.M., 2003. Using S/P amplitude ratios to constrain the focal mechanisms of small earthquakes. Bull. Seismol. Soc. Am. 93, 2434–2444.
Hariri, M.E., Abercrombie, R.E., Rowe, C.A., do Nascimento, A.F., 2010. The role of fluids in triggering earthquakes: observations from reservoir induced seismicity in Brazil. Geophys. J. Int. 181, 1566–1574.
Harris, R.A., 1998. Introduction to special section: stress triggers, stress shadows, and implications for seismic hazard. J. Geophys. Res. 103 (B10), 24347–24358.
He, X., Hong, T.-K., 2010. Evidence for strong ground motion by waves refracted from the Conrad discontinuity. Bull. Seismol. Soc. Am. 100 (3), 1370–1374.
Hickman, S., Sibson, R., Bruhn, R., 1995. Introduction to special section: mechanical involvement of fluids in faulting. J. Geophys. Res. 100 (B7), 12831–12840.
Hill, D.P., Reasenberg, P.A., Michael, A., Arabaz, W.J., Beroza, G., Brumbaugh, D., Brune, J.N., Castro, R., Davis, S., dePolo, D., Ellsworth, W.L., Gomberg, J., Harmsen, S., House, L., Jackson, S.M., Johnston, M.J.S., Jones, L., Keller, R., Malone, S., Munguia, L., Nava, S., Pechmann, J.C., Sanford, A., Simpson, R.W., Smith, R.B., Stark, M., Stickney, M., Vidal, A., Walter, S., Wong, V., Zollweg, J., 1993. Seismicity remotely triggered by the magnitude 7.3 Landers, California, earthquake. Science 260, 1617–1623.
Hong, T.-K., 2010. Lg attenuation in a region with both continental and oceanic environments. Bull. Seismol. Soc. Am. 100 (2), 851–858.
Hong, T.-K., Choi, H., 2012. Seismological constraints on the collision belt between the North and South China blocks in the Yellow Sea. Tectonophysics 570–571, 102–113.
Hong, T.-K., Kang, T.-S., 2009. Pn travel-time tomography of the paleo-continental-collision and rifting zone around Korea and Japan. Bull. Seismol. Soc. Am. 99 (1), 416–421.
Hong, T.-K., Rhie, J., 2009. Regional source scaling of the 9 October 2006 underground nuclear explosion in North Korea. Bull. Seismol. Soc. Am. 99 (4), 2523–2540.
Hong, T.-K., Baag, C.-E., Choi, H., Sheen, D.-H., 2008. Regional seismic observations of the 9 October 2006 underground nuclear explosion in North Korea and the influence of crustal structure on regional phases. J. Geophys. Res. 113, B03305. http://dx.doi.org/10.1029/2007JB004950.
Hough, S.E., Seeber, L., Armbruster, J.G., 2003. Intraplate triggered earthquakes: observations and interpretation. Bull. Seismol. Soc. Am. 93 (5), 2212–2221.
Houng, S.E., Hong, T.-K., 2013. Probabilistic analysis of the Korean historical earthquake records. Bull. Seismol. Soc. Am. 103 (5), 2782–2796.
Jaumé, S.C., Sykes, L.R., 1996. Evolution of moderate seismicity in the San Francisco Bay region, 1850 to 1993: seismicity changes related to the occurrence of large and great earthquakes. J. Geophys. Res. 101 (B1), 765–789.
Jiang, T., Peng, Z., Wang, W., Chen, Q.-F., 2010. Remotely triggered seismicity in continental China following the 2008 Mw 7.9 Wenchuan earthquake. Bull. Seismol. Soc. Am. 100 (5B), 2574–2589.
Jo, E., Hong, T.-K., 2013. Vp/Vs ratios in the upper crust of the southern Korean Peninsula and their correlations with seismic and geophysical properties. J. Asian Earth Sci. 66, 204–214.
Jun, M.-S., 1991. Body-wave analysis for shallow intraplate earthquakes in the Korean Peninsula and Yellow Sea. Tectonophysics 192, 345–357.
Keliang, Z., Jin, M., 2011. Numerical simulation of co-seismic deformation of 2011 Japan Mw9. 0 earthquake. Geodesy Geodyn. 2 (3), 16–23.
Kennett, B.L.N., Engdahl, E.R., Buland, R., 1995. Constraints on seismic velocities in the earth from travel times. Geophys. J. Int. 122, 108–124.
Kerr, R.A., 1993. Looking-deeply-into the Earths crust in Europe. Science 261, 295–297.
Kerr, R.A., 1994. German super-deep hole hits bottom. Science 266, 545.
Kerrich, R., La Tour, T.E., Willmore, L., 1984. Fluid participation in deep fault zones: evidence from geological, geochemical, and 180/60 relations. J. Geophys. Res. 89, 4331–4343.
Kilb, D., Gomberg, J., Bodin, P., 2000. Triggering of earthquake aftershocks by dynamic stresses. Nature 408, 570–574.
Kim, S.-K., Bae, T.-S., 2012. Analysis of crustal deformation on the Korea Peninsula after the 2011 Tohoku earthquake. J. Korean Soc. Surveying, Geodesy, Photogrammetry, Cartography 30 (1), 87–96 (in Korean).
King, G.C.P., Stein, R.S., Lin, J., 1994. Static stress changes and the triggering of earthquakes. Bull. Seismol. Soc. Am. 84 (3), 935–953.

Klein, F.W., 2007. User's Guide to HYPOINVERSE-2000. A Fortran Program to Solve for Earthquake Locations and Magnitudes. Open File Report 02.171 revised. Version 1.1. U.S. Geological Survey.
Lee, J., Hong, T.-K., 2014. Dynamic lithospheric response to megathrust and precursory seismicity features of megathrust. Phys. Earth Planet. Inter. 234, 35–45.
Lei, X., Xie, C., Fu, B., 2011. Remotely triggered seismicity in Yunnan, southwestern China, following the 2004 Mw9.3 Sumatra earthquake. J. Geophys. Res. 116, B08303. http://dx.doi.org/10.1029/2011JB008245.
Lin, J., Stein, R.S., 2004. Stress triggering in thrust and subduction earthquakes, and stress interaction between the southern San Andreas and nearby thrust and strike-slip faults. J. Geophys. Res. 109, B02303. http://dx.doi.org/10.1029/2003JB002607.
Ma, K.-F., Chan, C.-H., Stein, R.S., 2005. Response of seismicity to Coulomb stress triggers and shadows of the 1999 Mw=7.6 Chi-Chi, Taiwan, earthquake. J. Geophys. Res. 110, B05S19. http://dx.doi.org/10.1029/2004JB003389.
Mallman, E.P., Parsons, T., 2008. A global search for stress shadows. J. Geophys. Res. 113, B12304. http://dx.doi.org/10.1029/2007JB005336.
Mallman, E.P., Zoback, M.D., 2007. Assessing elastic Coulomb stress transfer models using seismicity rates in southern California and southwestern Japan. J. Geophys. Res. 112, B03304. http://dx.doi.org/10.1029/2005JB004076.
Matthews, M.V., Reasenberg, P.A., 1988. Statistical methods for investigating quiescence and other temporal seismicity patterns. Pure Appl. Geophys. 126, 357–372.
Miyazawa, M., 2011. Propagation of an earthquake triggering front from the 2011 Tohoku-Oki earthquake. Geophys. Res. Lett. 38, L23307. http://dx.doi.org/10.1029/2011GL049795.
Mooney, W.D., Ritsema, J., Hwang, Y.K., 2012. Crustal seismicity and earthquakes catalog maximum moment magnitude (Mcmax) in stable continental regions (SCRs): correlation with the seismic velocity of the lithosphere. Earth Planet. Sci. Lett. 357–358, 78–83.
Nalbant, S.S., 1998. Stress coupling between earthquakes in northwest Turkey and the north Aegean Sea. J. Geophys. Res. 103, 24469–24486.
Park, J.-C., Kim, W., Chung, T.W., Baag, C.-E., Ree, J.-H., 2007. Focal mechanisms of recent earthquakes in the southern Korean Peninsula. Geophys. J. Int. 169, 1103–1114.
Peng, Z., Gomberg, J., 2010. An integrated perspective of the continuum between earthquakes and slow-slip phenomena. Nat. Geosci. 3, 599–607.
Piombo, A., Martinelli, G., Dragoni, M., 2005. Post-seismic fluid flow and Coulomb stress changes in a poroelastic medium. Geophys. J. Int. 162, 507–515.
Rice, J.R., Gu, J.-C., 1983. Earthquake aftereffects triggering seismic phenomena. Pure Appl. Geophys. 121 (2), 187–218.
Saikia, C.K., 1994. Modified frequency-wavenumber algorithm for regional seismograms using Filon's quadrature; modeling of Lg waves in eastern North America. Geophys. J. Int. 118, 142–158.
Scholz, C.H., Sykes, L.R., Aggarwal, Y.P., 1973. Earthquake prediction: a physical basis. Science 181 (4102), 803–810.
Shelly, D.R., Peng, Z., Hill, D.P., Aiken, C., 2011. Triggered creep as a possible mechanism for delayed dynamic triggering of tremor and earthquakes. Nat. Geosci. 4, 384–388.
Sibson, R.H., 1985. A note on fault reactivation. J. Struct. Geol. 7 (6), 751–754.
Simpson, R.W., Schulz, S.S., Dietz, L.D., Burford, R.O., 1988. The response of creeping parts of the San Andreas fault to earthquakes on nearby faults: two examples. Pure Appl. Geophys. 126 (2–4), 665–685.
Stein, R.S., 1999. The role of stress transfer in earthquake occurrence. Nature 402, 605–609.
Sykes, L.R., 1978. Intra-plate seismicity, reactivation of pre-existing zones of weakness, alkaline magmatism, and other tectonics post-dating continental separation. Rev. Geophys. Space Phys. 16, 621–688.
Talwani, P., 2014. Intraplate Earthquakes. Cambridge University Press, New York (p. 332).
Talwani, P., Chen, L., Gahalaut, K., 2007. Seismogenic permeability, ks. J. Geophys. Res. 112, B07309. http://dx.doi.org/10.1029/2006JB004665.
Tinti, S., Mulargia, F., 1985. Effects of magnitude uncertainties on estimating the parameters in the Gutenberg–Richter frequency–magnitude law. Bull. Seismol. Soc. Am. 75, 1681–1697.
Toda, S., Enescu, B., 2011. Rate/state Coulomb stress transfer model for the CSEP Japan seismicity forecast. Earth Planets Space 63, 171–185.
Toda, S., Stein, R., 2003. Toggling of seismicity by the 1997 Kagoshima earthquake couplet: a demonstration of timedependent stress transfer. J. Geophys. Res. 108 (B12), 2567. http://dx.doi.org/10.1029/2003JB002527.
Toda, S., Stein, R.S., Richards-Dinger, K., Bozkurt, S.B., 2005. Forecasting the evolution of seismicity in southern California: animations built on earthquake stress transfer. J. Geophys. Res. 110, B05S16. http://dx.doi.org/10.1029/2004JB003415.
Toda, S., R.S. Stein, V. Sevilgen, J. Lin, 2011. Coulomb 3.3 Graphic-Rich Deformation and Stress-Change Software for Earthquake, Tectonic, and Volcano Research and Teaching- User Guide. U.S. Geological Survey. Open-File Report 2011–1060.
Waldhauser, F., Ellsworth, W.L., 2000. A double-difference earthquake location algorithm: method and application to the northern Hayward Fault, California. Bull. Seismol. Soc. Am. 90, 1353–1368.
West, M., Sánchez, J.J., McNutt, S.R., 2005. Periodically triggered seismicity at Mount Wrangell, Alaska, after the Sumatra earthquake. Science 308, 1144–1146.
Wiemer, S., Wyss, M., 2000. Minimum magnitude of completeness in earthquake catalogs: examples from Alaska, the Western United States, and Japan. Bull. Seismol. Soc. Am. 90 (4), 859–869.
Wu, C., Peng, Z., Wang, W., Chen, Q.-F., 2011. Dynamic triggering of shallow earthquakes near Beijing, China. Geophys. J. Int. 185, 1321–1334.
Wu, C., Gomberg, J., Ben-Naim, E., Johnson, P., 2014. Triggering of repeating earthquakes in central California. Geophys. Res. Lett. 41. http://dx.doi.org/10.1002/2013GL059051.
Yagi, Y., Fukahata, Y., 2011. Rupture process of the 2011 Tohoku-Oki earthquake and absolute elastic strain release. Geophys. Res. Lett. 38, L19307. http://dx.doi.org/10.1029/2011GL048701.
Zhao, B.W., Wang, S., Yang, M., Peng, X., Qiao, R.Du., Nie, Z., 2012. Far field deformation analysis after the Mw9.0 Tohoku earthquake constrained by cGPS data. J. Seismol. 16, 305–313.